A New Method of Ka DBF ATI-SAR for Full Ocean Current Vectors Inversion

Hui Wang, *Senior Member, IEEE*, Sili Wu, Qiang Zhao, Shichao Zheng, and Mingxi Xiao

***Abstract*—For applications such as high-precision current velocity field monitoring, Ka-band SAR has an important advantage in baseline configuration, which can be configured with dual antennas or more effective phase centers for a single satellite, forming omnidirectional current field measurement capabilities. However, the normalized radar cross section of the sea surface will decay rapidly with the larger incident angle, and it is difficult to obtain a high echo signal-to-noise ratio by active radiating method. Considering that the digital beamforming (DBF) scan on receive at a small incident angle will cause gain loss and phase error due to echo pulse extension and reduce the interferometric accuracy, this article proposes a dual-beam along-track interferometry (ATI) implementation architecture combined with pulse compression and channel forming, which has the advantages of bidirectional current velocity measurement capacity and compact hardware structure. Under a set of parameters, verified by simulation, it could be demonstrated that the proposed method has good robustness, can extract the velocity of the wide-swath current, and complete the extraction of the nongeotropic components. Moreover, the concept of DBF ATI-SAR was validated with airborne data.**

***Index Terms*—Along-track interferometry (ATI), digital beamforming (DBF), multichannel SAR, ocean current observation, scan on receive (SCORE).**

I. Introduction

THE total area of the ocean exceeds 70% of the global surface, and its dynamic and thermodynamic energy delivery is of great significance to the global climate, biological evolution, and prevention of meteorological disasters. Compared with the buoys and water stations that have been laid on a large scale, although the long-wave geostrophic component in the oceanic environment can be inverted using nadir altimetry, there is currently no mature space-based ocean current velocity measurement technology. SAR-based repeat-pass interferometry or long-baseline distributed interferometry is difficult to practice due to the decoherence of moving sea surface. Therefore, developing a current field measurement method and system based on single-satellite multichannel interferometry has significant meaning to geophysics. The full ocean current field includes geostrophic and nongeostrophic components. Extracting the nongeostrophic components is conducive to more accurate inversion of the direction of the full ocean current field.

Manuscript received 28 August 2022; revised 17 October 2022; accepted 27 October 2022. Date of publication 8 November 2022; date of current version 21 November 2022. *(Corresponding author: Mingxi Xiao.)*

The authors are with the Shanghai Key Laboratory of Aerospace Millimeter Wave Information Technology, Shanghai Satellite Engineering Institute, Shanghai 201109, China (e-mail: huiwang@mml-ciss.org; wslleo@163.com; zhaoqiangbuaa@163.com; jerryiszsc@163.com; xiaomingxi01@163.com).

Digital Object Identifier 10.1109/JSTARS.2022.3220292

The Ka-band millimeter wave has attracted extensive attention in the field of earth observation due to its short baseline advantage under the interferometric regime and sensitive characteristic sensitivity of backscattering surface [1], [2], [3]. The optimal interferometric baselines in the L, C, and other bands that require repeat-pass or multisatellites, which can be approximately optimal under the single Ka-satellite. However, according to the radar equation, the millimeter-wave band has high attenuation, and the Ka-band has not yet been widely used due to transmitter efficiency and atmospheric loss. In this regard, the millimeter-wave system based on digital beamforming (DBF) scan on receive (SCORE) technology can avoid the peak transmission power of tens of thousands of watts and achieve better measurement results, which has the potential to solve the space-based wide-field interpretation of submesoscale vortices and turbulent velocity vectors.

Beamforming technology has been used in the field of nonimaging radar for a long time and can greatly improve the signal-to-noise ratio (SNR) of the system and the corresponding accuracy [4], [5], [6]. Swath and high resolution are a pair of contradictory quantities. According to the principle of pulse radar, the high resolution along the range line is obtained by the high bandwidth, while the high resolution in the azimuth direction is restricted by the length of the antenna. However, the resolution cannot represent the full capability of the radar system, and a series of indicators including swath and SNR have important practical significance. For wide swath observation requirements, it is difficult to obtain good antenna gain in the entire width due to factors such as the broadening of the main lobe of the antenna pattern and the restriction of signal time width by range ambiguity, thereby reducing the SNR. For the realization of the wide-width system, not only can the beam steering method be used to measure the subswaths at different slant ranges to achieve wide-width, but also a multichannel configuration can be used to directly obtain multiple independent sampling data, through the ON-board or ON-ground forming to achieve overall signal quality improvement. By combining the DBF-SCORE technology, the DBF-SAR system has also undergone many theoretical researches and practices. Among them, the along-track interferometry (ATI) for vector velocity measurement based on the DBF system has attracted widespread attention. Corresponding system configurations are proposed [7]. However, in specific applications, the typical problems of DBF-SCORE include direction of arrival estimation, azimuth-variation, beam broadening, dispersion, echo channel amplitude and phase error, scanning grating lobe, and so on [8], [9].

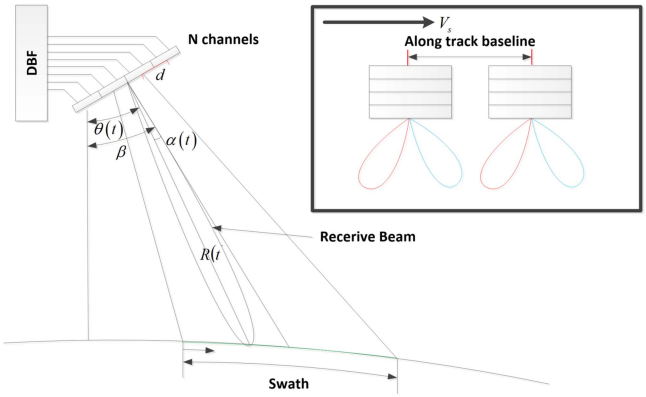

Fig. 1. Diagram of DBF-SCORE scanning.

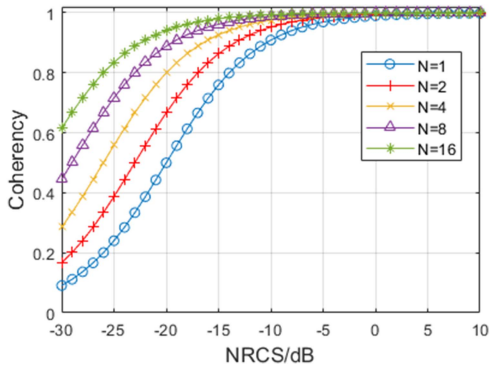

Fig. 2. Demonstration of image coherency after ideal forming.

Among them, according to the typical marine environment, there is only a small component of the macrotopography, and the azimuth-variation and the angle of arrival are not the core issues, therefore they are not within the scope of this article.

This article focuses on the accurate interpretation technology of ocean currents based on the millimeter wave frequency band, which can achieve the wide-swath vectorized inversion of geostrophic and nongeostrophic current fields through multichannel dual-beam interferometry, and analyzes the DBF structure for this purpose. In addition, the broadening and other error sources are analyzed in this article. Furthermore, the ON-board processing architecture and ground processing current suitable for the interferometry system have been clarified.

II. Principal Theory of DBF-ATI

DBF-SCORE technology is a multichannel solution for wide-swath observation, which is equipped with a small-aperture transmit antenna according to the corresponding relationship between beam width and antenna size. It also equips multiple small antennas at the receiving to meet the coverage of scenarios. The signal quality is improved by scanning-on receive at SCORE digital processor. It can provide sufficient system gain on the premise of avoiding excessive peak transmit power, which solves the problem of large loss in millimeter wave systems. The data of each channel is time-varying weighted and stacked. This method can always align the beam center of the digital receiving beam to the position of the pulse center during echo reception, thereby increasing the receiving gain. Moreover, the theoretical gain has been improved through channel-to-channel phase modulation. The Fig. 1 shows a schematic diagram of DBF-SCORE technology and range-oriented profile. According to the radar principle, the imaging swath under the fixed beam steering is determined by the beam main lobe width, the incident angle, and the platform height.

In the four-channel DBF system, as shown in Fig. 1, d is the antenna height, $\theta(t)$ is the ideal echo direction with fast time, β is the antenna normal direction, $\alpha(t) = \beta - \theta(t)$ is the angle difference between the echo and the antenna normal direction, that is, the scanning angle, $R(t)$ represents the slant range; Set W_r is the width of the swath along the slope distance; W_r is the echo near range; R_f is the far range; R_e is the radius of the earth. Due to the spatial position difference of the phase centers between the channels, there is a phase difference between the echoes naturally. After the ideal compensation, the signals between the channels can be accumulated in the same phase, which further increases the gain and improves the SNR. DBF-SCORE generates a scanning narrow receive beam. With ignoring the slow time and only analyzing the range time t, the forming signal could be represented as the vector sum of echo signal and SCORE weight coefficient

$$s(t) = \sum_{n=1}^{N} \omega_\mathrm{n}(t) \cdot s_\mathrm{n}(t) \tag{1}$$

where the echo signal of the n th aperture is $s_\mathrm{n}(t)$, and $\omega_\mathrm{n}(t)$ is the SCORE weight coefficient.

At the moment t, the beam steering $\alpha(t)$ is the angle between the center of the receiving beam and the antenna normal and corresponding direction of arrival is the theoretical direction

$$\theta\,(t) = arc\cos\left(\frac{4(H+R_\mathrm{e})^2 - 4R_\mathrm{e}^2 + (ct)^2}{4\,(H+R_\mathrm{e})\,ct}\right) \tag{2}$$

where H is the altitude of the satellite. c is the speed of propagation of electromagnetic waves, which is the speed of light.

Under ideal multibeam forming, the ability of the interferometric system will be extraordinarily improved. First, it can achieve a large swath through subapertures. And second, it can improve the total SNR by accumulating independent coherent signals. Under weak backscattering conditions, the phase error can be effectively suppressed. With a set of simulation parameters, the following coherence coefficients shown in Fig. 2 exist.

A. Pulse Extension Loss

As shown in Fig. 2, the interferometric phase of multiple channels can come into play when the echoes are weak, for ocean current scenarios. However, according to the literature [10], under the influence of the incident angle and the pulsewidth, the echo beam width will be broadened after the slant range-ground projection in the ideal model. The broadening echo beamwidth

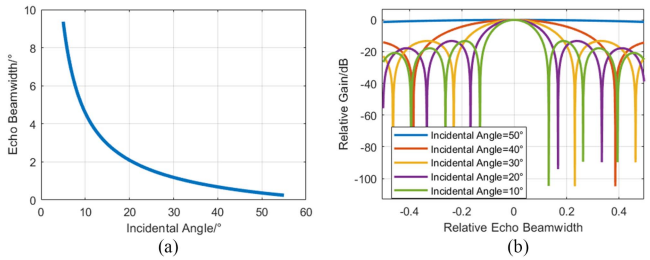

Fig. 3. Pulse extension phenomenon. (a) Echo beamwidth with different incident angles, where the receive window could be larger than the antenna beamwidth. (b) Relative Gain with relative beamwidth, where some of the data is sampled outside the main lobe.

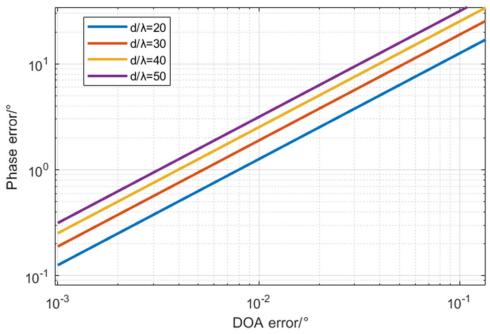

Fig. 4. Phase error with different DOA error.

is

$$\chi_\theta(\theta) = \frac{t_p c}{2R_a\left(\frac{R_a\cos(\theta)}{\sqrt{R_e^2-(R_a\sin(\theta))^2}}-1\right)\sin(\theta)} \tag{3}$$

where $R_a = H + R_e$ and t_p represents transmitted pulsewidth.

When the beam width exceeds the main lobe of the multichannel composite beam, gain loss occurs, and when the pulse extension loss (PEL) modulation depth is too large, further phase modulation occurs due to nonlinear amplitude. Fig. 3(a) shows the echo broadening with the change of the incident angle under the same pulsewidth, and Fig. 3(b) is the equivalent DBF antenna receiving pattern under the corresponding broadening.

B. Direction of Arrival Error

The weight factors used in DBF-SCORE technology are directly related to the direction of arrival (DOA). If the DOA error is large, it is equivalent to staggering the narrow scanning beam and the backscattering echo, and additional phase modulation will also be formed. According to the SCORE principle, the weight should be

$$\omega_{\mathrm{n}}(t) = \exp\left(-\mathrm{j}\frac{2\pi d_{\mathrm{n}}\sin(\alpha(t))}{\lambda}\right). \tag{4}$$

The phase errors with different DOA errors are shown in Fig. 4. At the same time, when the angle of arrival is estimated incorrectly, the center angle of the echo equivalent pattern within the width will be misaligned, resulting in a decrease in gain and

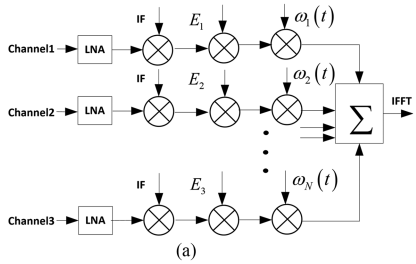

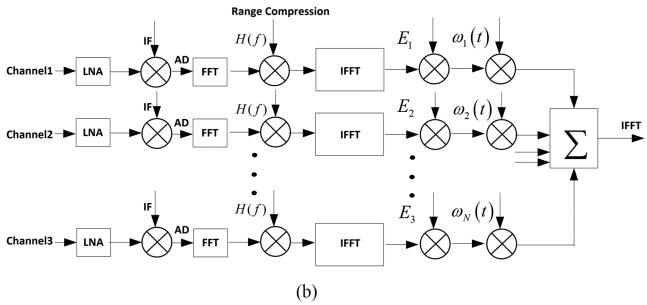

Fig. 5. DBF structures. (a) Procedures of original DBF-SCORE. (b) Procedures of DBF after independent range compression.

even deterioration in pulse compression performance and even secondary phase error modulation.

C. Fixed Amplitude and Phase Error

The fixed amplitude and phase error of the radio-frequency circuit of the multichannel system will affect the beam forming performance. Sampled data consists of noise and valid signal. Under single-channel processing, amplifying the entire digital signal cannot improve any performance. However, the intensity difference between channels will affect the contribution of the SNR after signal combination. Therefore, amplitude equalization should be completed without prior information. Similarly, the fixed phase calibration is also based on the basic assumption that the noise characteristic of the single-channel signal is gradually changing, so that the phase calibration can be performed with the phase of a certain point or a certain segment as a reference.

D. DBF Structures

We consider the DBF implementation of one of the two antennas, the echo beamwidth broadening, the angle of arrival error, the fixed amplitude, and phase error. First of all, the fixed amplitude and phase errors can be fixed by a high-precision internal calibrator. Fig. 5 shows two ways to achieve DBF as before pulse compression and after pulse compression, where LNA is a low noise amplifier and IF is a reference signal and E is a fixed amplitude phase error, $\omega(t)$ is SCORE weighted, $H(f)$ is the matching filter for the frequency domain.

For the traditional SCORE architecture in Fig. 5(a), the receive pattern is significantly affected by PEL for long time-width signals. The perfect solution is to use frequency-independent weighting coefficients to complete the modulation, but this operation is computationally expensive. In Fig. 5(b), the signal that is

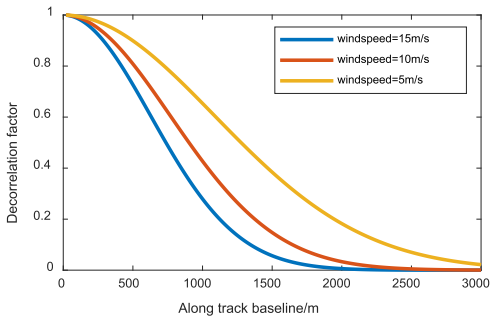

Fig. 6. Decorrelation factor caused by the baseline length at different wind speeds.

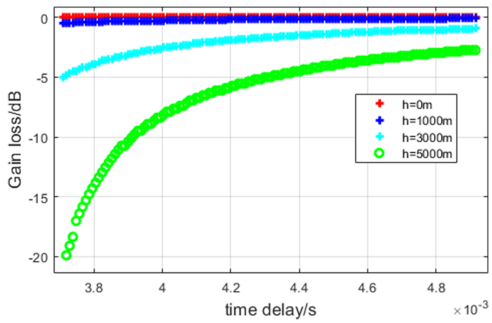

Fig. 7. Gain loss with different topography.

subjected to pulse compression processing first. The difference here is that the latter receiving pattern is essentially with the original small antenna. Therefore, for high-resolution or high-precision interferometric requirements, the second architecture has performance advantages and ON-board achievability.

III. Ocean Current Inversion Processing

The SAR data of the sea surface is directly related to the wind field speed [11], and the decoherence factor caused by the baseline length at different wind speeds is carried out in Fig. 6. The distributed system or repeat-pass InSAR is not suitable for high-precision ATI at strong wind speed. The gain loss caused by different terrain heights is shown in Fig. 7.

Due to the single-satellite interferometry, the phase modulation term for the estimation error of the DOA is removed and does not constitute a residual phase, but the gain loss directly causes the phase rms error to be increased. It could be found by simulation that it is much smaller than 1 dB of gain loss without estimating DOA for scenes for sea.

According to the literature [12], the ground transition component of the surface current field can be seen, which is determined by the dynamic topographic data of the sea surface, and the longitude velocity v and latitude velocity u in the nonequatorial region can be expressed as

$$v = -\frac{g}{2\gamma \sin\varphi}\frac{\partial D}{\partial x} \tag{5}$$

$$u = \frac{g}{2\gamma \sin\varphi}\frac{\partial D}{\partial y} \tag{6}$$

where g represents gravitational acceleration, γ is angular velocity of the Earth, φ is the dimension, x and y are the scale of the coordinate system, D is the height of the sea surface above a level surface, MSH is the mean sea height, and N is the geoid height.

Therefore, the mean sea surface elevation can be obtained through high-precision sea surface surveying and mapping, and the dynamic topography of the sea surface can be obtained by further calculating the difference with the geoid, and the geostrophic current can be obtained by the fitting model. At present, there is no direct space-based mapping source of non-geostrophic components, and the nongeostrophic components can be extracted from the omnidirectional velocity field measured by orbital interferometry by eliminating the above fitting data. In this regard, it needs to be clarified to what extent the accuracy of sea surface elevation can be meaningful. According to the accuracy of the existing mean dynamic topography (MDT) model, measurement capabilities of gravity satellites and altimeter satellites for the geoid and ocean dynamic surface, it can be found that the realization of wide-scale data at the kilometer scale can play a role [13]. The analysis of the InSAR accuracy is not within the scope of this article, and it will not be carried out in detail. The application of single-satellite high-coherency multibaseline data has the ability to achieve submesoscale sea surface mapping. The related Ka-band systems and processing analysis work can refer to related work [14], [15].

Based on the abovementioned analysis, an interferometric method based on DBF-SCORE is proposed, which extracts the speed information of the region by means of pulse compression, DBF synthesis, imaging, registration, phase extraction, and geostrophic component removal, as shown in Fig. 8.

In the ideal dual beam case, the interferometric phase of the target by the velocity is the equation

$$(v_{fo}, v_{ba}) = \left(\frac{2\pi}{\lambda}\frac{B_{\mathrm{x}}}{V_p\phi_{fo}}, \frac{2\pi}{\lambda}\frac{B_{\mathrm{x}}}{V_p\phi_{ba}}\right) \tag{7}$$

where v_{fo} and v_{ba} are the orthogonal velocity component, B_{x} is along the track baseline, V_p is the satellite velocity, and ϕ_{fo} and ϕ_{ba} are the interferometric phase and under omnidirectional beams, respectively.

IV. Experiments and Discussion

In order to evaluate the proposed DBF ATI-SAR concept, here, a set of Ka-band SAR parameters are provided, ocean dynamic model modeling and numerical simulation are conducted, and the extraction of the 2-D flow field is completed. The processing method has been verified by airborne millimeter-wave SAR data.

A. Ka-Band DBF ATI-SAR Parameters

Unlike the spatial baseline required for cross-track interferometry, along track interferometry requires the observation geometry that is as consistent as possible between a coherent data pair. The SAR imaging principle shows that the azimuth resolution comes from Doppler modulation, and the directly measurable baseband Doppler comes from the stable relative

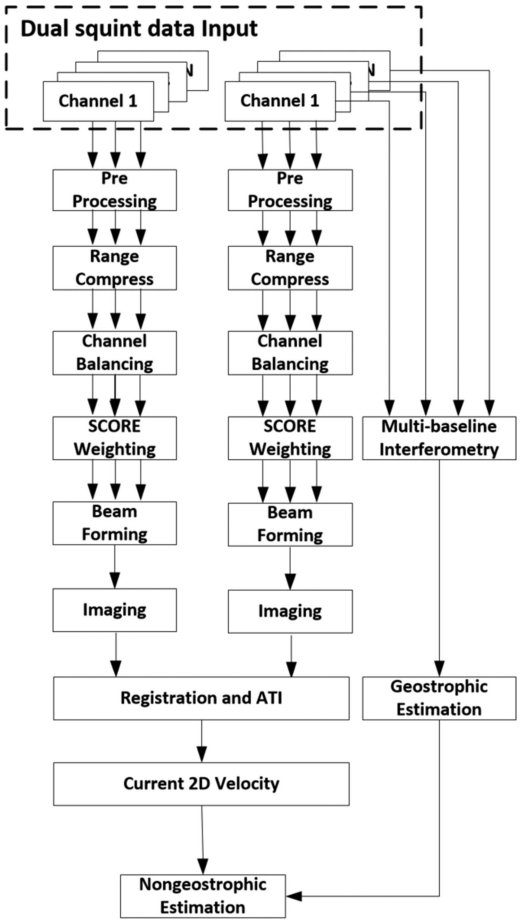

Fig. 8. Flowchart of proposed method.

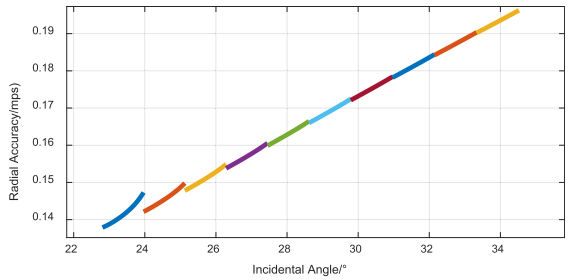

Fig. 9. Relationship between the total ATI speed measurement performance of the system and incident angle.

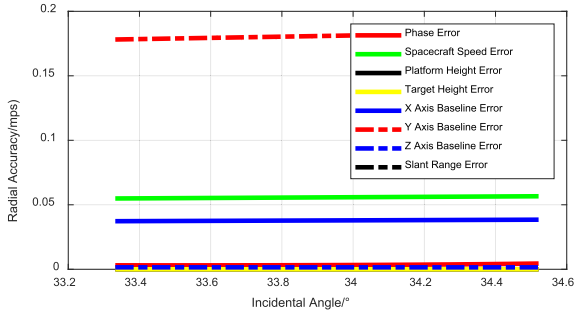

Fig. 10. Relationship between ATI accuracy and incident angle in a subswath.

motion between the ground stationary target and the linear moving platform. When the target is accompanied by radial velocity during the synthetic progress, an additional phase modulation from that of the stationary target is bound to be added to the phase term.

As known, the baseline setting is the core indicator of interferometric SAR, in which a long baseline can achieve greater phase difference accumulation under the same observation geometry, and obtain better interferometric sensitivity; while a short baseline along the track avoids high temporal decoherence. In other context, it can be found that the ideal baseline lengths for different frequency bands are quite different, and it is difficult to deploy the optimal baselines for X, C, or L frequency bands through one satellite. The moving current is different from the stationary land, and its velocity component will cause the temporal coherence to deteriorate rapidly. Therefore, it is much more difficult to achieve ocean-oriented ATI through a distributed platform than a monostatic system. It could be referred to for the baseline set toward our application purpose. When the baseline length is less than 20 m, the coherence factor can be guaranteed to be greater than 0.95 in any sea state. Here, considering the feasibility, the distance between DBF antennas is set as 16 m and it serves as the length of the interferometric baseline. Moreover, since the cross-track interferometric phase of the cross-track cannot be removed the by a robust processing method in the hybrid-baseline scenario, it is only necessary to keep the baseline along the track as much as possible when setting the initial parameters. In this regard, single-satellite InSAR has the unparalleled advantage of being able to directly couple the vertical baseline component to the spacecraft attitude control ability.

In order to achieve a lower random noise level by multilook, a radio frequency bandwidth of 200 MHz is used, which can meet the needs of refined sea surface phenomenon observation. It is worth noting that although a large bandwidth can obtain better resolution characteristics, it will also form a larger receiver noise power on the RF chain according to the radar equation, so it needs to be weighed according to the expected spatial resolution of the product and the system cost. Because of the characteristics of the backscattering of the sea surface, the orbital consideration here is how to achieve an enough swath first, and then the radiated power. According to the backscattering characteristics of the water surface in the Ka-band, even a small average power can achieve a strong echo for velocity retrieval. Since there is basically no specific strong point target in the ocean, the ambiguity ratio can be relatively loose.

Table I shows the system parameters used to analyze the effect of multichannel beamforming ATI on speed measurement performance. The noise equivalent sigma zero (NESZ) is the decisive parameter of SNR incoherence. Range-ambiguity-to-signal ratio (RASR) and azimuth ambiguity-to-signal ratio (AASR) are two important parameters in SAR system design, which affect the imaging performance of the system.

Interferometric accuracy can be divided into random errors and systematic errors, where the latter usually manifests as a bias. The radial velocity measurement accuracy can be differentiated to obtain the contribution of the error subitem, and the sum of the squares can represent the overall interferometric velocity

TABLE I
SIMULATION PARAMETER INPUTS

System parameters	The parameter value
Carrier Frequency	35.75 GHz
Track height	900 km
Swath width	400 km
Bandwidth	200 MHz
Transmit antenna height	0.2 m
Receive antenna height	0.2 m
The number of receive channels	N=8
The length of the transceiver antenna	5 m
X-axis baseline length	16 m
Y-axis baseline length	0 m
Z-axis baseline length	0 m
Single-channel NESZ	0 dB
RASR	-25 dB
AASR	-20 dB
Grid	50 m×50 m

measurement capability. Define the x-axis heading DBF-ATI system in the $x-y-z$ coordinate system, A_1 and A_2 represent two pairs of multichannel receiving antennas along the track with a baseline B, a is the sum of the orbit height H and the earth's radius, θ is the incident angle. Speed measurement accuracy is

$$\sigma_{V_\mathrm{r}}=\sqrt{\begin{array}{l}\left(\frac{\partial V_\mathrm{r}}{\partial V_\mathrm{P}}\right)^2\sigma_V^2+\left(\frac{\partial V_\mathrm{r}}{\partial B}\right)^2\sigma_B^2+\left(\frac{\partial V_\mathrm{r}}{\partial \Phi_{12}}\right)^2\sigma_{\Phi_{12}}^2\\ +\left(\frac{\partial V_\mathrm{r}}{\partial B_\mathrm{y}}\right)^2\sigma_{B_\mathrm{y}}^2+\left(\frac{\partial V_\mathrm{r}}{\partial B_\mathrm{z}}\right)^2\sigma_{B_\mathrm{z}}^2+\left(\frac{\partial V_\mathrm{r}}{\partial h}\right)^2\sigma_\mathrm{h}^2\\ +\left(\frac{\partial V_\mathrm{r}}{\partial a}\right)^2\sigma_\mathrm{a}^2+\left(\frac{\partial V_\mathrm{r}}{\partial R}\right)^2\sigma_{\mathrm{r}_0}^2.\end{array}} \tag{8}$$

The error sources $\sigma_{V_\mathrm{P}},\sigma_B,\sigma_{\Phi_{12}},\sigma_{\mathrm{B_y}},\sigma_{\mathrm{B_z}},\sigma_\mathrm{h},\sigma_\mathrm{a},\sigma_{\mathrm{r}_0}$ mean the measurement uncertainty of the spacecraft speed, the baseline length along the track, the interference phase, the baseline y-axis, the baseline z-axis, the height of the observation scene, the height of the orbit, the observation slant range, and the contribution factors of each error, which are expressed as

$$\frac{\partial V_\mathrm{r}}{\partial V_\mathrm{P}}=\frac{1}{B}\left(\frac{\lambda}{2\pi}\Phi_{12}-B_\mathrm{z}\cos\theta-B_\mathrm{y}\sin\theta\right) \tag{9}$$

$$\frac{\partial V_\mathrm{r}}{\partial S_\mathrm{V}}=-\frac{2v_\mathrm{amb}}{\lambda B}\left(\frac{\lambda}{2\pi}\Phi_{12}-B_\mathrm{z}\cos\theta-B_\mathrm{y}\sin\theta\right) \tag{10}$$

$$\frac{\partial V_\mathrm{r}}{\partial \Phi_{12}}=\frac{v_\mathrm{amb}}{\pi} \tag{11}$$

$$\frac{\partial V_\mathrm{r}}{\partial B_\mathrm{y}}=\frac{2v_\mathrm{amb}}{\lambda}\sin\theta \tag{12}$$

$$\frac{\partial V_\mathrm{r}}{\partial B_\mathrm{z}}=\frac{2v_\mathrm{amb}}{\lambda}\cos\theta \tag{13}$$

$$\frac{\partial V_\mathrm{r}}{\partial h}=-\frac{2v_\mathrm{amb}r_\mathrm{e}}{\lambda a r_0}\left(B_\mathrm{z}+\frac{1}{\tan\theta}B_\mathrm{y}\right) \tag{14}$$

$$\frac{\partial V_\mathrm{r}}{\partial a}=-\frac{2v_\mathrm{amb}}{\lambda}\left(\frac{1}{r_0}-\frac{\cos\theta}{a}\right)\left(B_\mathrm{z}+\frac{1}{\tan\theta}B_\mathrm{y}\right) \tag{15}$$

$$\frac{\partial V_\mathrm{r}}{\partial r_0}=-\frac{2v_\mathrm{amb}}{\lambda}\left(\frac{1}{a}-\frac{\cos\theta}{R}\right)\left(B_\mathrm{z}+\frac{1}{\tan\theta}B_\mathrm{y}\right). \tag{16}$$

When the multilook number is N_L, the interferometric phase can be expressed as

$$\hat{\phi}=\arctan\left[\frac{\mathrm{Im}\left\{\sum_{n=1}^{N_L}s_1^{(n)}s_2^{*(n)}\right\}}{\mathrm{Re}\left\{\sum_{n=1}^{N_L}s_1^{(n)}s_2^{*(n)}\right\}}\right] \tag{17}$$

where s_1 ands_2, respectively, represent the complex signal after multichannel beamforming, and the standard deviation of the interferometric phase is

$$\sigma_{\Phi_{12}}=\frac{1}{\sqrt{2N_\mathrm{L}}}\frac{\sqrt{1-\gamma^2}}{\gamma}. \tag{18}$$

And previously is a function of the coherence coefficient. The total coherence coefficient can be expressed as the product of subcorrelation coefficients

$$\gamma=\gamma_\mathrm{tgt}\cdot\gamma_\mathrm{dop}\cdot\gamma_\mathrm{pro}\cdot\gamma_\mathrm{asr}. \tag{19}$$

Among them, $\gamma_\mathrm{tgt}\cdot\gamma_\mathrm{dop}\cdot\gamma_\mathrm{pro}\cdot\gamma_\mathrm{asr}$ represent the target SNR coherence coefficient, spatial coherence coefficient, Doppler coherence coefficient, processing coherence coefficient, and ambiguity coherence coefficient, respectively. The echo signal-to-noise is greatly affected by the multichannel beamforming process in range, mainly including channel fixed phase error, spatial decoherence, beam pointing error, and arrival angle error. The three factors reduce the SNR and affect the quality of the output signal, thereby reducing the effect of ATI.

Considering the SAR along-track image pair of the same scene, the corresponding arbitrary pixel data a_1 and a_2 are

$$a_1=s_1+n_1 \tag{20}$$

$$a_2=s_2+n_2. \tag{21}$$

Interferometry signal s_1 and s_2 has a phase difference ϕ_v

$$s_2=s_1\exp\left(-j\phi_\mathrm{v}\right). \tag{22}$$

Under ideal conditions, n_1 and n_2 are independent noises. Then, the coherence coefficient for this pixel is

$$\gamma_{tgt}=\frac{\langle a_1a_2^*\rangle}{\sqrt{\langle a_1a_1^*\rangle\langle a_2a_2^*\rangle}}. \tag{23}$$

After removing the irrelevant terms, (23) can be expressed as

$$\gamma_{tgt}=\frac{\langle s_1s_2^*\rangle}{\sqrt{\left(\langle s_1s_1^*\rangle+\langle n_1n_1^*\rangle\right)\left(\langle s_2s_2^*\rangle+\langle n_2n_2^*\rangle\right)}}. \tag{24}$$

Simplified as follow:

$$\gamma_{tgt}=\frac{S\exp\left(j\phi_\mathrm{v}\right)}{S+N}=\frac{\exp\left(j\phi_\mathrm{v}\right)}{1+1/\mathrm{SNR}}\approx\frac{1}{1+1/\mathrm{SNR}} \tag{25}$$

where

$$N = \langle n_1 n_1^* \rangle = \langle n_2 n_2^* \rangle ; S = \langle s_1 s_1^* \rangle = \langle s_2 s_2^* \rangle \quad (26)$$

$$S \exp(j\phi_v) = \langle s_1 s_2^* \rangle . \quad (27)$$

Thermal noise is the main element of incoherent noise. Define the radar cross section of the observed target in the radar echo as σ_{tgt}, and the equivalent backscattering coefficient of the radar system as σ_0. Then, the logarithm of (28) is obtained, and the target SNR along the incident angle

$$G_{tgt} = \sigma_{tgt} - \sigma_0. \quad (28)$$

The DBF signal is obtained as

$$s_{dbf}(t) = \sum_{n=1}^{N} s_n(t). \quad (29)$$

It can be found that when there is a fixed phase error in each channel signal of the DBF receiving system, which will not directly affect the energy accumulation caused by single-channel pulse compression. However, after multichannel forming, cancellation will be formed in each corresponding range bin. Define the fixed phase gain loss as

$$G_p = 10 \log 10 \left(\frac{S_{dbf}}{N S_{ref}} \right) \quad (30)$$

$$S_{dbf} = \langle s_{dbf} s_{dbf}^* \rangle ; S_{ref} = \langle s_{ref} s_{ref}^* \rangle . \quad (31)$$

When the ground has height fluctuations, the angle of arrival estimation obtained by the ideal flat earth geometry has a non-negligible error. The direction pointed by the SCORE method is defined as $\theta_s(t)$. θ_0 is the direction of the echo of the real target with elevation h, then the angle estimation error is

$$\Delta\theta = \theta_0 - \theta_s(t_0) \quad (32)$$

where t_0 is the two-way time delay of the echo and no echo is received by the maximum gain of the multichannel forming, according to the ideal state. Because the gain is lost due to the terrain. G_0 is the equivalent pattern of the receiving antenna, and the loss is expressed as

$$G_l = \frac{G_0(\theta_s + \Delta\theta)}{G_0(\theta_s)}. \quad (33)$$

Under the ideal flying configurations, the effects of spatial decoherence for an interferometric system along the track can usually be ignored, but for multichannel systems, due to the difference in the incident angle caused by the cross track baseline, it will cause the inherent signal difference of the radar echo and reduce the coherence on a spatial scale. The spatial gain loss under multichannel, expressed as

$$G_{spatial} = 10 \log 10 \left(1 - \frac{2 \cos\theta |\delta\theta| \rho_y}{\lambda} \right) \quad (34)$$

where ρ_y is the distance resolution, then the maximum viewing angle difference $\delta\theta$ between channels is about $(N-1)d/r_0$. The SNR of the DBF-SAR image is

$$\mathrm{SNR} = G_{tgt} + G_p + G_l + G_{spatial}. \quad (35)$$

Under the abovementioned design, it can be obtained that the InSAR has overall performances as shown in Fig. 9.

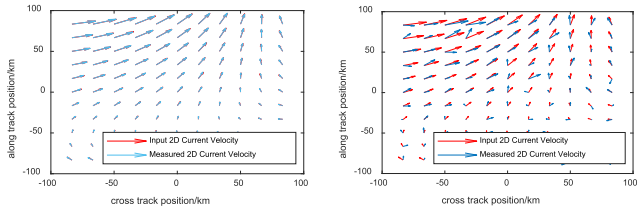

Fig. 11. Two-dimensional velocity inversion (incident angle = 20°). (a) Measured velocity by DBF after compression. (b) Measured velocity by DBF before compression.

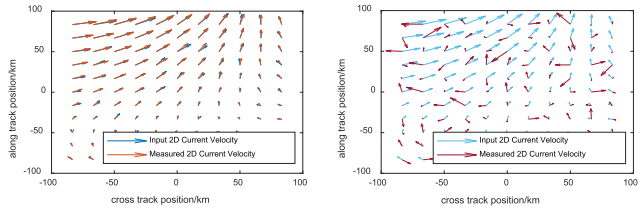

Fig. 12. Two-dimensional velocity inversion (incident angle = 10°). (a) Measured velocity by DBF after compression. (b) Measured velocity by DBF before compression.

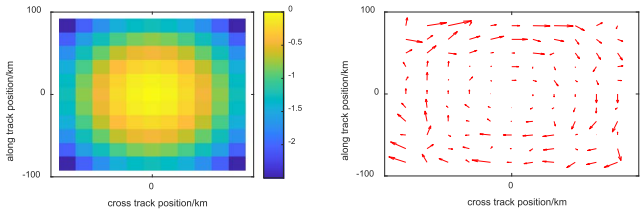

Fig. 13. Across track interferometric result. (a) Measured sea surface height by multichannel baselines. (b) Measured geostrophic current.

By decomposing the accuracy of one of the subswaths, the following error with the incident angle is obtained in Fig.10.

B. Simulation Experiment and Performance Analysis

The simulation uses a 2-D swath of 200 km and an input speed range from 0 to 3 m/s, and with the speed component caused by the undulating height of sea surface, the selection of the velocity range is within the velocity ambiguity. As shown in the Fig. 11, the unidirectional velocity measurement of the two DBF implementations at a 20° angle of incidence can be found to be directly reflected in the speed measurement accuracy. By consistent sea surface normalized radar cross section parameters, the speed measurement error in Fig. 11(a) has an average error of 4.7% with respect to the input amount, while the average error is 11.5% in (b).

Furthermore, reduce the incident angle and keep the same pulsewidth. According to previous content, the echo beamwidth broadening increases at a small incident angle. It can be found that the speed parameter accuracy of DBF processing after pulse compression is obviously better than that of direct DBF by

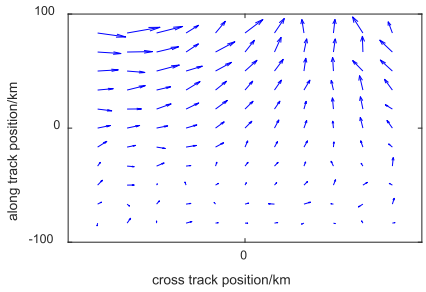

Fig. 14. Measured nongeostrophic current.

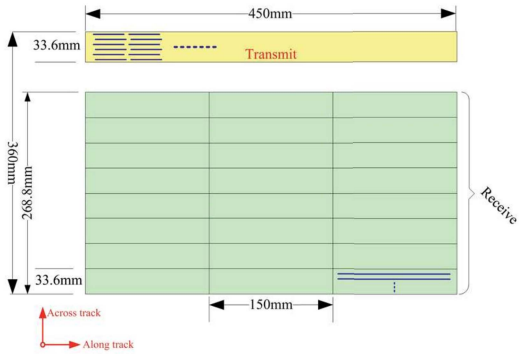

Fig. 15. Antenna configuration.

baseband echo. The latter has been unable to achieve effective speed measurement in Fig. 12.

Through multibaseline interferometry, the topographic relief of 40 000 km^2 in this area is obtained in Fig. 13 (assuming that the absolute elevation can be calibrated by an external DSM model, only the relative measurement accuracy is considered here).

The mean sea surface height has been calculated by topography, the difference with the geoid was calculated, and the circulation velocity caused by MDT was obtained by further inversion. By taking the difference in the total velocity vector, the geostrophic component and the nongeostrophic component can be obtained by fitting, as shown in Fig. 14.

C. Airborne Results

To validate the DBF-SCORE-ATI method, an airborne test has been carried out. The airborne millimeter-wave InSAR system is as follows. There are 3 sets of 8-subarray along the track, which can form the longest baseline of 0.3 m. The bandwidth of the SAR system is 200 MHz, as shown in Fig. 15, the height of the transmitting antenna is 0.0336 m and the length is 0.45 m; the height of the receiving antenna is 0.0336 m and the length is 0.15 m.

Using the four-channel DBF technology, we have embedded digital sampling, digital down-conversion, filtering, and range compression processing in the hardware system. However, although this system also has the beam forming function under ideal conditions, due to the uncertainty of the airborne flight attitude, the calibration between channels is difficult. Compensation and DBF work is still done in the digital signal processing stage. A larger theoretical echo gain can be obtained, therefore,

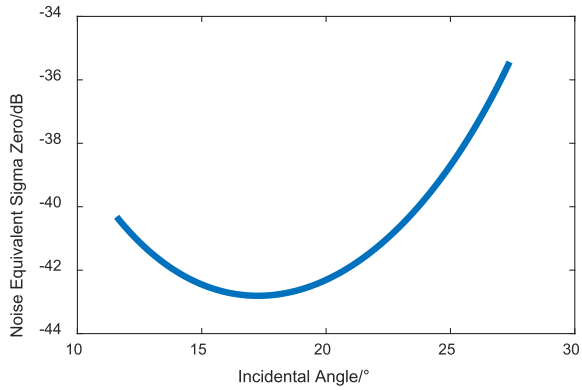

Fig. 16. Simulation results of noise equivalent sigma zero variation with incident angle.

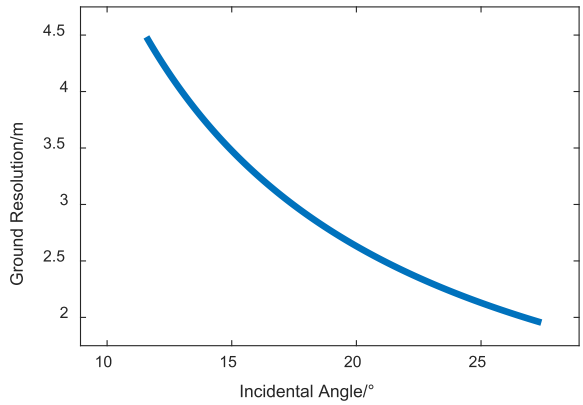

Fig. 17. Simulation results of Ground resolution variation with incident angle.

it is not necessary to use an incident angle below 10° and the echo window is approximately 12° to 26°. As shown in Fig. 16, the full width has an equivalent sensitivity better than −35 dB in the case of multichannel forming, and it is expected that a pair of images along the track with a high enough SNR can be achieved, so that the Interferometric information extraction is finally completed.

As shown in Fig. 17, the overall resolution along the ground is better than 5 m, and the image has a certain interpretability at this incident angle.

As shown in Fig. 18 , the distance blur is low, which meets the requirements of interference imaging.

The theoretical speed measurement accuracy of the prototype system Fig. 19 is better than 0.5 m/s. And the ATI accuracy allocation in a sub-swath is shown in Fig. 20.

The observation effect of SAR comes directly from the data products, and most of the SAR data products are based on SAR images that have been well-focused in two dimensions. Both mission requirements and platform characteristics place specific demands on SAR imaging processing. The overall trajectory of spaceborne SAR is stable. However, due to the trajectory is macroscopically nonlinear, it is necessary to quantitatively correct the slant range model in ultrahigh-resolution imaging. During airborne SAR imaging, the aircraft is greatly affected by airflow, vehicle stability, and pilot operations, and there will be high-frequency jitter and low-frequency three-axis rolling.

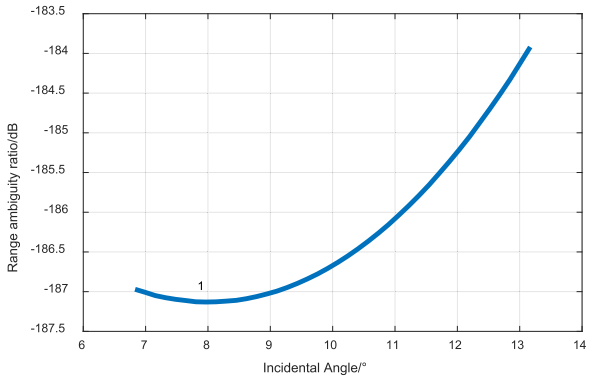

Fig. 18. Simulation results of range ambiguity ratio variation with incident angle.

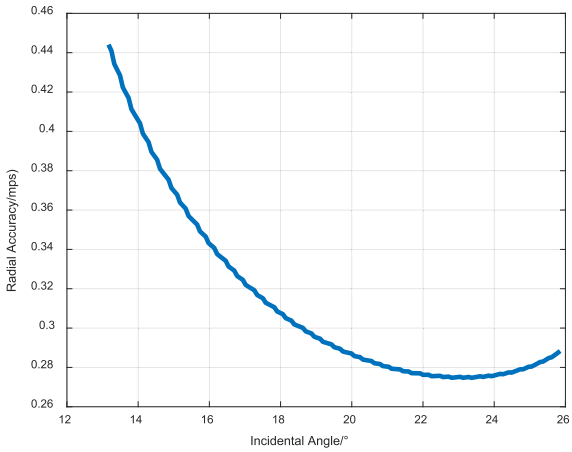

Fig. 19. Theoretical speed measurement accuracy of the prototype system.

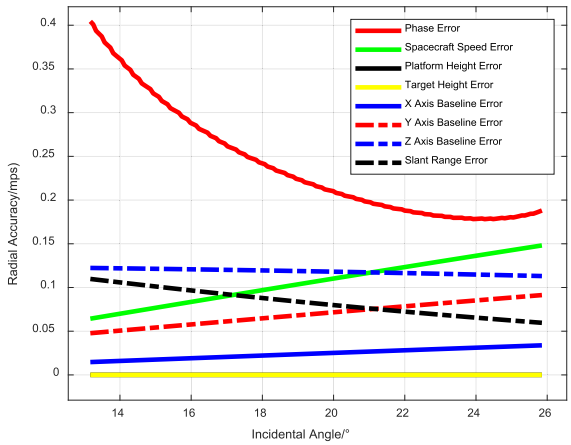

Fig. 20. ATI accuracy allocation in a subswath.

Due to the instability of the motion platform, the image quality will inevitably decrease, which needs to be compensated and corrected accordingly. Fundamentally, due to the constancy of the speed of light, SAR imaging is a correction of the relationship between slant range-phase-time and it is related to the fact that SAR data forms a highly coherent and continuous distance in the

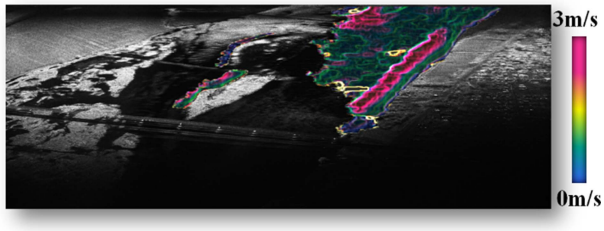

Fig. 21. ATI result.

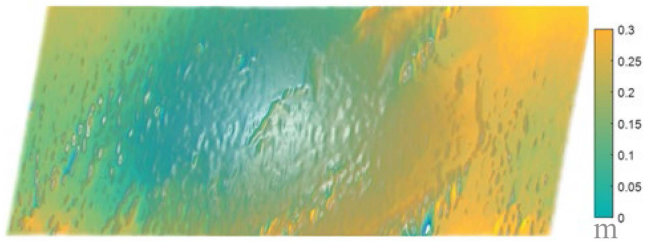

Fig. 22. Cross-track Interferometry result.

dimensions of fast time-slow time-multiple acquisitions. In the direction-azimuth-coherent processing interval relationship, if the SAR is offset or split in any continuous process of position and three-dimensional attitude when the measured data is acquired, it will greatly increase the difficulty of signal processing. In the practical application of range multichannel, there are two main purposes, the one is the InSAR signal processing based on the cross-track baseline component, the other is multichannel beamforming to improve the quality of multichannel signals as much as possible in order to maintain InSAR information. In an absolutely ideal situation, independent sampling data can be effectively formed and gaussian noise can be randomly canceled, and the ideal signal quality can be obtained by DBF.

Due to the design relationship between the baseline and the wavelength, in the millimeter wave band, the baseline can be easily observed along the track at the decimeter level to achieve airborne interferometry along track and obtain the speed information of the scene. Under the condition of nonsquint interferometric acquisition in strip mode, the static component of the scene echo meets the zero doppler condition. With the four-channel DBF-SCORE technology. The results in Fig. 21 are obtained after signal processing and calibration. It can be found that the speed extraction conforms to the basic topography of the scene, showing a clear distinction at the river bank, and because of the shallow water flow, there is no obvious speed information on the tidal flats and shoals. The water velocity along the river bank is higher, and the river center velocity is lower. The measurement accuracy is verified by the current meter, which is better than 0.1 m/s.

Fig. 22 is obtained by interferometric processing of the SAR data of the above river through the cross-track baseline formed by subarrays. The results of water surface altimetry are verified by multiple calibration points, and the accuracy is better than 0.3 m.

V. Conclusion

In this section, DBF-SAR could improve the interferometric performance of the system in the weak scattering environment. In terms of specific implementation, real-time pulse compression, and synthesis of multichannel radar data can improve the along-track interference performance in case of small incident angles or long pulsewidths, and 2-D current velocity inversion can be performed by interchannel interferometric phase extraction. Furthermore, the geostrophic component extraction is used to realize the refined inversion of quantitative products. Under the same time width and 10° incident angle, the velocity measurement accuracy can be improved from 11.5 to 4.7% compared to the DBF after pulse compression. When the speed is relatively large and close to the ambiguity speed, it can also be proposed by the fitting of the geostrophic speed to improve the speed aliasing. Future work will focus on refined current modeling and measured data processing to implement an evaluation of the detailed design in this article.

References

[1] H. Wang, F. Zhao, and Y. Deng, "Development and application of the millimeter wave SAR," *J. Infrared MillimeterWaves*, vol. 34, no. 4, pp. 452–459, 2015.

[2] H. Wang, H. Zhang, S. Dai, and Z. Sun, "Azimuth multichannel GMTI based on Ka-band DBF-SCORE SAR system," *IEEE Geosci. Remote Sens. Lett.*, vol. 15, no. 3, pp. 419–423, Mar. 2018.

[3] S. Biancamaria, D. P. Lettenmaier, and T. M. Pavelsky, "The SWOT mission and its capabilities for land hydrology," *Surv. Geophys.*, vol. 37, no. 2, pp. 307–337, 2016.

[4] W. Xu et al., "Onboard digital beamformer with multi-frequency and multi-group time delays for high-resolution wide-swath SAR," *Remote Sens,* vol. 13, no. 21, 2021, Art. no. 4354.

[5] N. Gebert, M. Villano, G. Krieger, and A. Moreira, "Errata: Digital beamforming on receive: Techniques and optimization strategies for high-resolution wide-swath SAR imaging," *IEEE Trans. Aerosp. Electron. Syst.*, vol. 49, no. 3, pp. 2110–2110, Jul. 2013.

[6] H. Wang, S. Wu, and S. Zheng, "Dual-Mode interferometric experiment using Ka DBF-SAR," in *Proc. 2nd China Int. SAR Symp.*, 2021, pp. 1–4, doi: 10.23919/CISS51089.2021.9652204.

[7] S. Wollstadt, P. López-Dekker, F. De Zan, and M. Younis, "Design principles and considerations for Spaceborne ATI SAR-Based observations of ocean surface velocity vectors," *IEEE Trans. Geosci. Remote Sens.*, vol. 55, no. 8, pp. 4500–4519, Aug. 2017.

[8] A. A. Jneibi, M. Abououf, H. Saleh, L. Alrahis, T. Assaf, and T. Stouraitis, "Application specific design for digital beam-former (DBF)," in *Proc. 24th IEEE Int. Conf. Electron., Circuits Syst.*, 2017, pp. 111–115, doi: 10.1109/ICECS.2017.8292038.

[9] Q. Zhao et al., "On the frequency dispersion in DBF SAR and digital scalloped beamforming," *IEEE Trans. Geosci. Remote Sens.*, vol. 58, no. 5, pp. 3619–3632, May 2020.

[10] M. Younis, T. Rommel, F. Bordoni, G. Krieger, and A. Moreira, "On the pulse extension loss in digital beamforming SAR," *IEEE Geosci. Remote Sens. Lett.*, vol. 12, no. 7, pp. 1436–1440, Jul. 2015.

[11] O. G. Nwogu and D. R. Lyzenga, "Surface-Wavefield estimation from coherent marine radars," *IEEE Geosci. Remote Sens. Lett.*, vol. 7, no. 4, pp. 631–635, Oct. 2010.

[12] J. A. Knauss and N. Garfield. *Introduction to Physical Oceanography*. Long Grove, IL, USA: Waveland Press, 2016.

[13] B. Xi-xuan, Y. Hao-ming, Z. Yao-zhong, P. Peng, and S. Ying-chun, "Progress in mean dynamic topography and geostrophic current research based on satellite geodetic techniques," *Prog. Geophys.,* vol. 31, no. 5, pp. 2063–2071, 2016.

[14] R. Morrow et al., "Global observations of fine-scale ocean surface topography with the surface water and ocean topography (SWOT) mission," *Front. Mar. Sci.*, vol. 6, 2019, Art. no. 232.

[15] M. Durand, L.-L. Fu, D. P. Lettenmaier, D. E. Alsdorf, E. Rodriguez, and D. Esteban-Fernandez, "The surface water and ocean topography mission: Observing terrestrial surface water and oceanic submesoscale eddies," *Proc. IEEE*, vol. 98, no. 5, pp. 766–779, May 2010.

[16] A. C. H. Martin, C. P. Gommenginger, and Y. Quilfen, "Simultaneous ocean surface current and wind vectors retrieval with squinted SAR interferometry: Geophysical inversion and performance assessment," *Remote Sens. Environ.*, vol. 216, pp. 798–808, 2018.

[17] J. Qiu et al., "A novel weight generator in real-time processing architecture of DBF-SAR," *IEEE Trans. Geosci. Remote Sens.*, vol. 60, 2022, Art. no. 5204915.

[18] Z. Chen, Z. Zhang, W. Wang, Q. Zhao, Y. Wen, and X. Meng, "Performance demonstration of dispersive SCORE: Digital scalloped beamforming with X-Band and C-Band DBF-SARs," *IEEE Geosci. Remote Sens. Lett.*, vol. 19, 2022, Art. no. 4016905.

[19] F. He, X. Ma, Z. Dong, and D. Liang, "Digital beamforming on receive in elevation for multidimensional waveform encoding SAR sensing," *IEEE Geosci. Remote Sens. Lett.*, vol. 11, no. 12, pp. 2173–2177, Dec. 2014.

[20] F. Queiroz de Almeida, M. Younis, G. Krieger, and A. Moreira, "An analytical error model for Spaceborne SAR multichannel azimuth reconstruction," *IEEE Geosci. Remote Sens. Lett.*, vol. 15, no. 6, pp. 853–857, Jun. 2018.

[21] Y. Chen, M. Huang, Y. Zhang, C. Wang, and T. Duan, "An analytical method for dynamic wave-related errors of interferometric SAR ocean altimetry under multiple sea states," *Remote Sens.*, vol. 13, no. 5, Mar. 2021, Art. no. 986.

[22] S. Huber, M. Younis, A. Patyuchenko, G. Krieger, and A. Moreira, "Spaceborne reflector SAR systems with digital beamforming," *IEEE Trans. Aerosp. Electron. Syst.*, vol. 48, no. 4, pp. 3473–3493, Oct. 2012.

[23] I. Sikaneta, C. H. Gierull, and D. Cerutti-Maori, "Optimum signal processing for multichannel SAR: With application to high-resolution wide-swath imaging," *IEEE Trans. Geosci. Remote Sens.*, vol. 52, no. 10, pp. 6095–6109, Oct. 2014.

[24] W. Wang et al., "Improved digital beam-forming approach with scaling function for range multi-channel synthetic aperture radar system," *IET Radar Sonar Navigation*, vol. 10, pp. 379–385, 2016.

[25] G. Krieger et al., "Advanced digital beamforming concepts for future SAR systems," in *Proc. IEEE Int. Geosci. Remote Sens. Symp.*, 2010, pp. 245–248, doi: 10.1109/IGARSS.2010.5650516.

[26] M. Reza et al., "Design and performance estimation of a photonic integrated beamforming receiver for Scan-on-Receive synthetic aperture radar," *J. Lightw. Technol.*, vol. 39, no. 24, pp. 7588–7599, Dec. 2021.

[27] M. Younis, F. Q. de Almeida, M. Villano, S. Huber, G. Krieger, and A. Moreira, "Digital beamforming for spaceborne reflector-based synthetic aperture radar, part 1: Basic imaging modes," *IEEE Geosci. Remote Sens. Mag.*, vol. 9, no. 3, pp. 8–25, Sep. 2021.

[28] M. Younis, F. Q. de Almeida, F. Bordoni, P. López-Dekker, and G. Krieger, "Digital beamforming techniques for multi-channel synthetic aperture radar," in *Proc. IEEE Int. Geosci. Remote Sens. Symp.*, 2016, pp. 1412–1415, doi: 10.1109/IGARSS.2016.7729361.

[29] F. Queiroz de Almeida, M. Younis, G. Krieger, and A. Moreira, "Multichannel staggered SAR azimuth processing," *IEEE Trans. Geosci. Remote Sens.*, vol. 56, no. 5, pp. 2772–2788, May 2018.

[30] P. Cheng, J. Wan, Q. Xin, Z. Wang, M. He, and Y. Nian, "An improved azimuth reconstruction method for multichannel SAR using vandermonde matrix," *IEEE Geosci. Remote Sens. Lett.*, vol. 14, no. 1, pp. 67–71, Jan. 2017.

Hui Wang (Senior Member, IEEE) was born in Harbin, China, in 1972. She received the Ph.D. degree in communication and information system from Harbin Institute of Technology, Harbin, China, in 2009.

She was engaged in research on advanced technologies related to synthetic aperture radar for a long time. She is a well-known expert in the field of SAR and a pioneer in the field of spaceborne millimeter wave SAR in China. She is currently the chief technical director of Shanghai Academy of Spaceflight Technology, Shanghai, China, in the field of millimeter wave SAR system, as well as the Director with SAST Millimeter Wave Imaging Laboratory and Shanghai Key Laboratory of Aerospace Millimeter Wave Information Technology, Shanghai, China. She is also a doctoral supervisor with both Harbin Institute of Technology and Shanghai Jiao Tong University, Shanghai, China, the Vice Chairman of IEEE Geoscience and Remote Sensing Society Shanghai Branch, as well as the editorial board member of Shanghai Aerospace Magazine for part-time jobs.

Sili Wu was born in Hebei, China, in 1996. He received the M.Eng. degree in information and communication engineering from the Shanghai Academy of Spaceflight Technology, Shanghai, China, in 2020.

He is an Engineer with the Shanghai Key Laboratory of Aerospace Millimeter Wave Information Technology. His research interests include SAR system design and signal processing, millimeter wave interferometric SAR signal processing, and its applications.

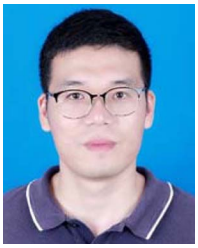

Qiang Zhao was born in Shandong, China, in 1989. He received the M.Eng. degree in instrument science and technology from Beihang University, Beijing, China, in 2014.

He is currently a Senior Engineer with the Shanghai Key Laboratory of Aerospace Millimeter Wave Information Technology. His research interests include radar signal processing, millimeter wave SAR data processing, and application.

Shichao Zheng was born in Shandong, China, in 1986. He received the Ph.D. degree in communication and information system from the University of Chinese Academy of Sciences, Beijing, China, in 2014.

He is currently the Deputy Director Millimeter Wave Imaging Laboratory, Shanghai Institute of Aerospace Technology, Shanghai, China, as well as the Senior Engineer with Shanghai Key Laboratory of Aerospace Millimeter Wave Information Technology, Shanghai, China. His research interests include SAR system design and signal processing, and millimeter wave interferometric SAR signal processing.

Mingxi Xiao was born in Jiangxi, China, in 1998. He is currently working toward the master's degree in information and communication engineering with the Shanghai Institute of Aerospace Technology, Shanghai, China.

His current research interests include millimeter wave interferometric SAR signal processing, SAR system design, and signal processing.